Biomed Microdevices (2010) 12:223–233
DOI 10.1007/s10544-009-9377-6

Handheld histology-equivalent sectioning laser-scanning confocal optical microscope for interventional imaging

Karthik Kumar · Rony Avritscher · Youmin Wang · Nancy Lane · David C. Madoff · Tse-Kuan Yu · Jonathan W. Uhr · Xiaojing Zhang

Published online: 10 December 2009

Abstract A handheld, forward-imaging, laser-scanning confocal microscope (LSCM) demonstrating optical sectioning comparable with microtome slice thicknesses in conventional histology, targeted towards interventional imaging, is reported. Fast raster scanning (~2.5 kHz line scan rate, 3.0–5.0 frames per second) was provided by a 2-axis microelectromechanical system (MEMS) scanning mirror fabricated by a method compatible with complementary metal-oxide-semiconductor (CMOS) processing. Cost-effective rapid-prototyped packaging combined the MEMS mirror with micro-optical components into a probe with 18 mm outer diameter and 54 mm rigid length. ZEMAX optical design simulations indicate the ability of the handheld optical system to obtain lateral resolution of 0.31 and axial resolution of 2.85 μm. Lateral and axial resolutions are experimentally measured at 0.5 μm and 4.2 μm respectively, with field of view of 200×125 μm. Results of reflectance imaging of *ex vivo* swine liver, and fluorescence imaging of the expression of cytokeratin and mammaglobin tumor biomarkers in epithelial human breast tissue from metastatic breast cancer patients are presented. The results indicate that inexpensive, portable handheld optical microscopy tools based on silicon micromirror technologies could be important in interventional imaging, complementing existing coarse-resolution techniques to improve the efficacy of disease diagnosis, image-guided excisional microsurgery, and monitored photodynamic therapy.

Keywords Handheld instrumentation · Laser scanning confocal microscope (LSCM) · CMOS-compatible scanning micromirror · Microelectromechanical systems (MEMS) · Interventional imaging

K. Kumar · Y. Wang
Department of Electrical and Computer Engineering,
University of Texas at Austin,
1 University Station C0803,
Austin, TX 78712, USA

R. Avritscher · D. C. Madoff
Section of Interventional Radiology,
University of Texas M. D. Anderson Cancer Center,
1515 Holcombe Boulevard,
Houston, TX 77030, USA

N. Lane · J. W. Uhr
Cancer Immunobiology Center,
University of Texas Southwestern Medical Center at Dallas,
5323 Harry Hines Boulevard,
Dallas, TX 75390, USA

T.-K. Yu
Radiation Treatment Center,
University of Texas M. D. Anderson Cancer Center,
1515 Holcombe Boulevard,
Houston, TX 77030, USA

X. Zhang (✉)
Department of Biomedical Engineering,
University of Texas at Austin,
1 University Station C0800,
Austin, TX 78712, USA
e-mail: John.Zhang@engr.utexas.edu

1 Introduction

Miniaturized depth-resolved optical imaging can enable highly sensitive biopsy-free characterization of diseases *in situ* and precision guided microsurgery and photodynamic therapy at improved spatial resolution, augmenting existing image-guided intervention methods such as magnetic resonance or ultrasound imaging (Yaqoob et al. 2006). Laser-scanning confocal microscopy (LSCM) allows high-

resolution imaging of an "optical section" situated a few hundred micrometers beneath the tissue surface, enabling visual tumor assessment in the epithelium by mapping spatial variations in refractive index of native tissue or detecting fluorescent markers preferentially bound to tumor sites. Axial resolution of 5 μm or less, comparable to the thickness of microtome slices in conventional histology and less than that of a single layer of cells, is required to ensure high contrast while imaging in highly scattering media such as biological tissue (Rajadhyaksha et al. 1999). Achieving the cellular-scale optical sectioning in a compact and versatile forward-imaging miniature probe, which has not been achieved in previous literature, would facilitate its application in surgical operating theaters and *in vivo* clinical studies. Microelectromechanical system (MEMS) technologies are uniquely suited to combining actuators for guiding light in very small volumes with micro-optical elements for *in vivo* beam scanning and imaging. The scaling laws in optics enable miniaturized imaging probes with functionality that cannot practically be achieved with traditional technologies (Solgaard 2008). Micromirrors powered by electrostatic vertical comb drives (Dooyoung et al. 2004; Hyuck et al. 2007; Krishnamoorthy et al. 2003) provide the favorable optical characteristics, large deflection angles and fast response times required for real-time imaging, and have been employed in optical coherence tomography (Aguirre et al. 2007; Woonggyu et al. 2005; Kumar et al. 2008a), confocal (Maitland et al. 2006; Ra et al. 2008; Kumar et al. 2008b) and multi-photon (Hoy et al. 2008; Piyawattanametha et al. 2006; Fu et al. 2006) microscopies. Unfortunately, the micromirrors used in these studies have been fabricated by complicated micromachining processes, resulting in low wafer yield, non-linear transformation between input voltage and mechanical scan angle and unstable scanning characteristics due to a significant tendency to exhibit the pull-in phenomenon and cease scanning operation. MEMS design processes that integrate complementary metal-oxide-semiconductor (CMOS) circuitry on the same chip as the MEMS device are widely seen as the solution to this problem, and have gained significant attention in recent years (Cheng et al. 2005; Ching-Liang et al. 2005; Dai et al. 2005; Fedder et al. 2008). We have addressed these drawbacks by introducing a simple 3-mask comb self-aligned micromirror fabrication process compatible with traditional CMOS processing in the semiconductor industry (Kumar et al. 2009a). Our process only utilizes conventional silicon processing tools which operate at temperatures low enough to allow pre-fabrication of CMOS circuitry on the wafer prior to commencing micromirror fabrication. For microendoscopes, this can enable CMOS-MEMS integration of control electronics and sensors to adaptively correct for aberrations in beam scanning along with power amplifier drive electronics, while significantly reducing fabrication costs and lowering the barriers towards clinical applications and market acceptance. Based on this fast-scanning two-axis MEMS micromirror, we report in this paper, for the first time, a handheld forward-imaging confocal microscope capable of sub-micrometer lateral resolution and optical sectioning comparable to histology, and demonstrate its application to reflectance and fluorescence imaging of the native spatial variation of refractive index contrast of biological tissues and expression of molecular tumor biomarkers respectively.

2 Methods

2.1 LSCM instrumentation

We have developed a handheld forward-imaging single-fiber laser-scanning confocal microscope incorporating our fast high-reflectivity two-axis micromirror in the distal scanning mechanism. The single-fiber approach provides high-quality pixilation-free imaging and a simple approach to aligning the confocal pinhole to the image of the point on the sample created by the objective system (Kimura and Wilson 1991). The schematic of the optical layout of our system is provided in Fig. 1. The semiconductor diode

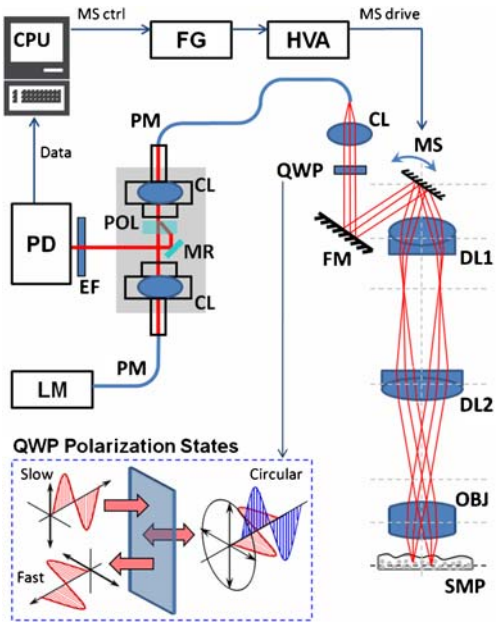

Fig. 1 Schematic of the optical layout of the single-fiber laser-scanning confocal microscope. LM: laser module; PM: polarization-maintaining single-mode fiber; CL: collimating lens; QWP: quarter-wave plate; FM: folding mirror; MS: micromirror scanner; DL1: doublet beam expander lens 1; DL2: doublet beam expander lens 2; OBJ: objective lens; SMP: sample being imaged; POL: walk-off polarizer; MR: miniature reflector; EF: emission filter; PD: photo-detector; CPU: central processing unit; FG: function generator; HVA: high-voltage amplifier

laser module LM (Blue Sky Research, Inc., FMXL-635-017-PA-0B), operating at a wavelength of 635 nm and maximum power of 17 mW, launches linearly polarized light into a polarization maintaining single-mode fiber PM, with the electric field of the coherent laser light oriented along the slow axis of the PM fiber. The PM fiber terminates at an optical bench (OFR, Inc., FT-38x100-3 W) housing the components to extract light reflected from the sample. Light exiting the fiber is coupled into a second PM fiber (Oz Optics, Inc., LPC-01-635-4/125-P, 0.11 NA) through two identical collimating lenses CL (OFR, Inc., PAF-X-5-VIS) and a calcite walk-off polarizer POL (OFR, Inc., PB-5x7-16-VIS). The polarizer ensures that only light of polarization aligned to the slow axis the PM fibers enters the second fiber. The core of the second PM fiber is 4.0 μm in diameter; therefore the exit aperture of the second PM fiber serves as the confocal pinhole in our system by virtue of its small size. This light diverges out of the exit aperture of the second fiber into the distal-end optical system. The still linearly-polarized light diverging from the fiber is collimated into a quarter-wave plate QWP by a miniature 5 mm effective focal length (EFL) aspheric lens mounted at the collimator end of the second PM fiber, which has the diameter of 1 mm, matching the size of the micromirror scanner in our system. The QWP (Red Optronics, Inc., 0.1"×0.1" Zero-Order MicroWaveplate) converts the light linearly polarized along the slow axis of the PM fiber into circularly polarized light, as shown in the inset in Fig. 1. The circularly polarized light is deflected by the folding mirror onto the micromirror scanner in a folded optical path, for compactness. The micromirror scanner is positioned at the back focal plane of a doublet lens DL1 (Thorlabs, Inc., AC050-008-A1) and deflects the beam across its entrance aperture in raster fashion. The doublet lens DL1 is part of an afocal Keplerian beam expander system, acting in conjunction with doublet lens DL2 (Thorlabs, Inc., AC127-025-A1-ML). The doublet lens DL1 converts the angular deflection created by the micromirror scanner into linear deflection of the focused spot in the intermediate focal plane. The position of the back focal plane of doublet lens DL2 is adjusted to match this intermediate focal plane. Doublet lens DL2 reconverts the linear scan into angular scan about a pivot point located at the point on the optical axis intersecting with the front focal plane of DL2. In effect, the beam expander increases the full-width half maximum (FWHM) diameter of the laser beam by a factor of about 3× in order to almost fill the back aperture of the objective lens OBJ, thereby maximizing the object-space numerical aperture (NA) of the distal optical system. In addition to increasing the object-space NA, the beam expander also translates the real pivot point, i.e., the micromirror scanner, to a virtual pivot point located at the back focal plane of the objective lens OBJ. This action results in the objective lens OBJ (Thorlabs, Inc., 350390-B, Ø4 mm, 2.75 mm EFL, 0.68 NA) converting the angular scan about the virtual pivot point into a linear scan across the sample.

The focused and scanned spot on the sample induces direct backscatter due to native spatially-varying refractive index contrast present in the sample, or induces emission (enhanced reflective backscatter) from fluorophores (reflective contrast agents) selectively tagged to tumor biomarkers at the imaging site. The reflective backscatter is known to maintain its original circularly polarized state while the fluorescence emission has components of all polarization states. The polarization-maintaining property of reflective backscatter is exploited to improve the signal-to-noise ratio in reflection confocal imaging mode (Gan et al. 1999; Schmitt et al. 1992). The backscattered light retraces its path through the distal optical system and the QWP. At this point, the circularly polarized reflective backscatter is converted linearly polarized light, this time however, aligned along the fast axis of the PM fibers. Any spurious reflection from a part of the optical system prior to the QWP is therefore easily distinguished from the signal we wish to detect from the sample by analyzing its polarization. The QWP has no significant effect on fluorescent emission from the sample. The reconverted light is coupled into the PM fiber through the CL lens that acts as a focuser. Only light backscattered (or created, in the case of fluorescence) from the sample plane that was confocal with the aperture of the PM fiber enters into the fiber, and out-of-focus light is rejected at the PM fiber entrance, yielding confocal action. The spatially filtered light propagates through the PM fiber and into the proximal end of the system, where it is collimated by the lens CL on fiber table, and into the polarizer POL. The polarizer separates the polarization aligned along the fast and slow axes of the fiber. The slow axis polarization is rejected, while the fast axis light is reflected off a miniature reflector into an emission filter. For reflectance imaging, the emission filter is removed, while in fluorescence imaging, the emission filter eliminates the laser line and allows any fluorescence to enter into the photodetector (New Focus, Inc., Model 2051-FS).

The circuitry that drives the micromirror scanner and synchronized data collection is controlled by a central processing unit (CPU). The CPU controls the amplitude and phase of the 2-channel function generator FG (Tektronix, Inc., AFG3022B), which outputs two drive signals corresponding to two-axis scanning and their associated trigger pulses in synchrony. The voltages of the drive signals output by the FG are amplified by a factor of 50× by a high-voltage amplifier HVA (TEGAM, Inc., Model 2350) before being supplied to the micromirror scanner. The first drive signal operates at the resonant frequency of the inner axis of the micromirror scanner to create fast line scans, while the second

signal varies slowly at the frame rate required for imaging. The pulses trigger the recording of samples from the photodetector by the data acquisition board (National Instruments, Inc., NI PCI-6111). Data samples are acquired only during the forward line and frame traces of the micromirror, while image processing is performed in real time during the acquisition idle time in the retrace scanning segment. All data acquisition, signal processing, and image rendering is performed in a Matlab® graphical user interface (GUI) program loaded in the CPU.

2.2 Scanning micromirror

Our scanning micromirror was the core component (labeled MS in Fig. 1 enabling the probe, and was fabricated by a simple method (Kumar et al. 2009a) that is compatible with the complementary metal-oxide-semiconductor (CMOS) processes employed in the electronics industry. CMOS-compatible processing can allow on-chip integration of sensors and electronics to improve scanning precision, wafer yield and device lifetimes, while reducing fabrication costs and barriers to commercial market acceptance (Ching-Liang et al. 2005; Fedder et al. 2008). The mirrors (Fig. 2) measured 1,024 μm in diameter and were fabricated on chips of size 2.8 mm^2. Out-of-plane rotation about two orthogonal axes intersecting at the mirror center, based on a gimbal design, was generated by two pairs of electrostatic staggered vertical comb drives on each axis. Primary resonances for the mechanical structure were observed at around 2.8 kHz and 670 Hz for the two rotation axes. Mechanical deflection angles of 11° and 6° at these resonant peaks were observed on the fast and slow axes respectively. When applying static or low-frequency voltages, maximum double-sided deflection angles of 5° and 4.5°, respectively, were obtained. Raster scanning was achieved by operating the fast axis at resonance to perform line scans, and applying a low-frequency sinusoidal voltage to the slow axis, creating frame scans. Image data was acquired only during forward traces of line and frame scans, with frame retrace being utilized for real-time image processing prior to display. Trigger waveforms from the signal generators synchronized the Matlab® image acquisition code with micromirror position.

2.3 Handheld forward-imaging probe

Forward imaging was achieved in the probe by aiming coherent illumination out of the single-mode polarization-

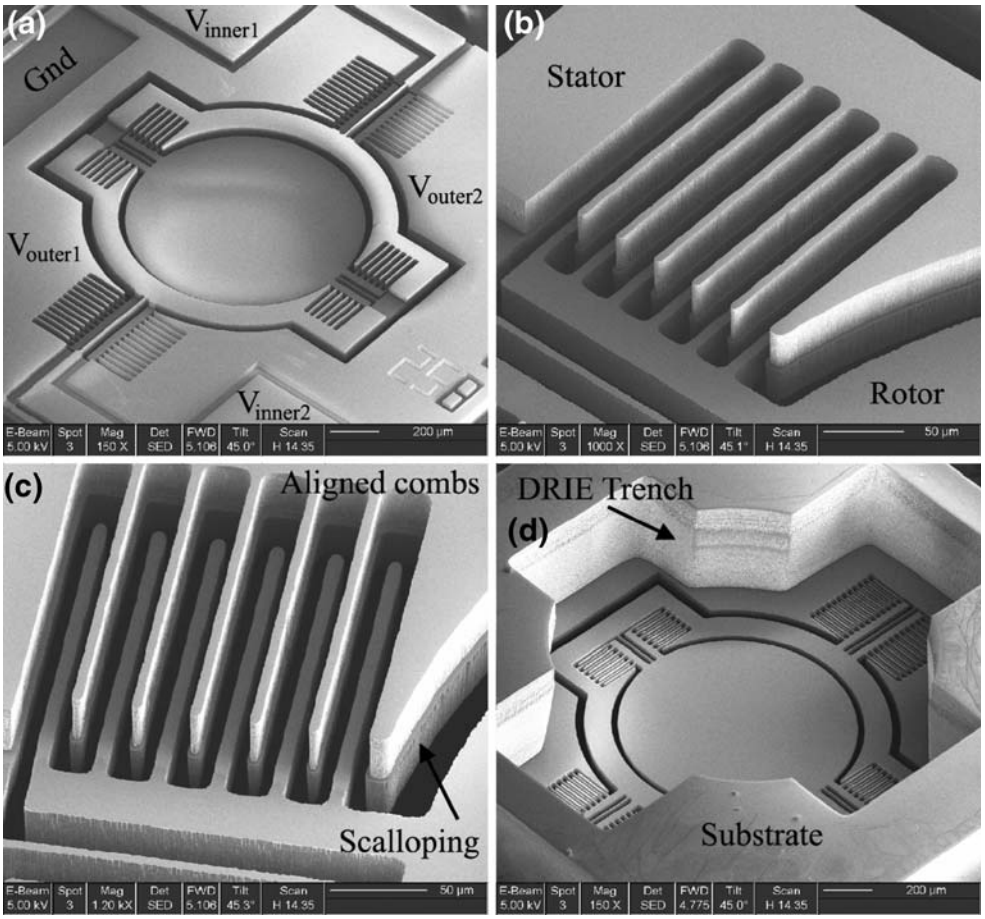

Fig. 2 Scanning electron micrograph (SEM) images of the fabricated devices. (**a**) Top view of micromirror showing electrical bond pads, comb drives on both axes, and micromirror surface. (**b**) Close-in view of layers forming the combdrive actuator on the inner axis. (**c**) Close-in view of the quality of alignment between the stator and rotor comb fingers. (**d**) Backside view of the substrate DRIE through-etch, bottom face of the micromirror

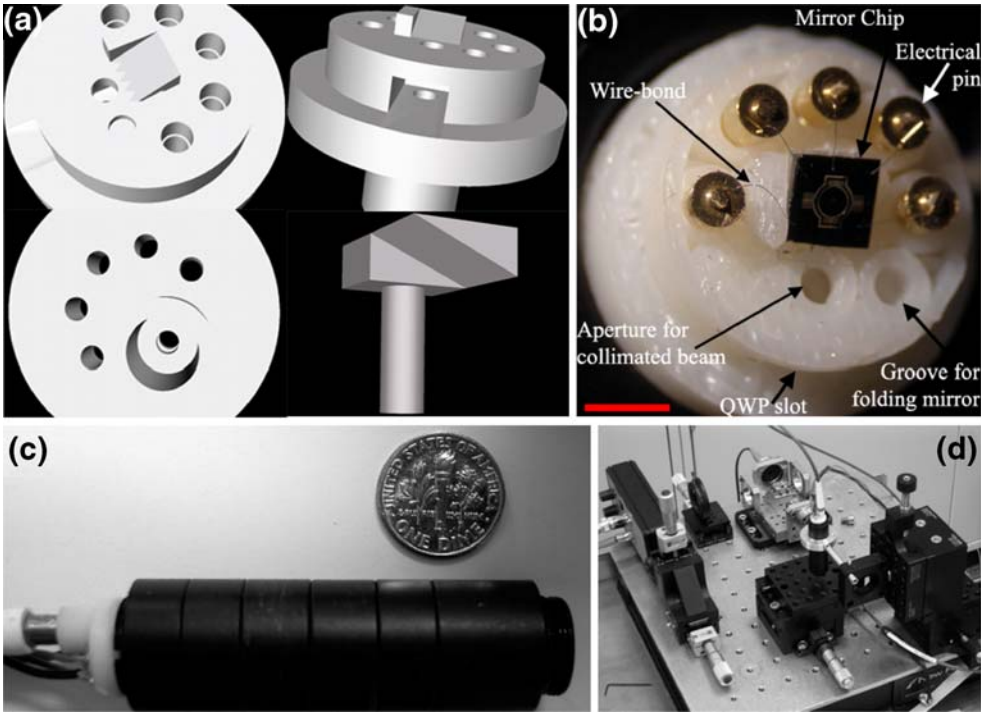

Fig. 3 Design and assembly of the handheld forward-imaging probe. (**a**) Mechanical drawings of the MEMS mount with top, bottom, and oblique views of main component depicted along with the folding mirror. (**b**) Photograph of the fabricated mount with a micromirror packaged in it. (**c**) Photograph of the fully assembled handheld probe. (**d**) Photograph of the portable system instrumentation

maintaining fiber with pigtailed collimator at a stationary mirror, which deflected it onto the micromirror in a folded optical path (Kumar et al. 2009b). We developed a cost-effective MEMS probe package fabricated by laser stereolithography rapid prototyping to combine the micromirror with the other optical components. The use of inexpensive batch-fabricated components in the distal system was motivated by the clinical considerations for a probe that can eventually be made disposable after one-time use. The package (Fig. 3(a–b)) included a hollow tube 4 mm inner diameter to secure the collimator, mounted stationary mirror, inclined surface to mount the micromirror chip, vias for five electrical pins to power the micromirror, threading to attach the objective system and position the micromirror at its back focal plane, and a slot to introduce a miniature QWP into the beam path with appropriate orientation. The QWP could alternatively be incorporated further ahead in the optical path within the objective system for improved noise rejection.

Our objective system was assembled using standard 1/2" tube lens optics (Thorlabs, Inc.). Attaching the module to the MEMS package with compatible threading completed assembly of the final system (Fig. 3(c–d)). The objective consisted of a Keplerian beam expander providing 3× magnification of spot size followed by a high numerical aperture (NA) aspheric lens serving as the focusing element. The focusing lens had 0.65 NA when its 3.6 mm clear aperture was filled by the entering beam. The micromirror diameter determined the maximum size of the beam entering the objective, and was designed such that the back

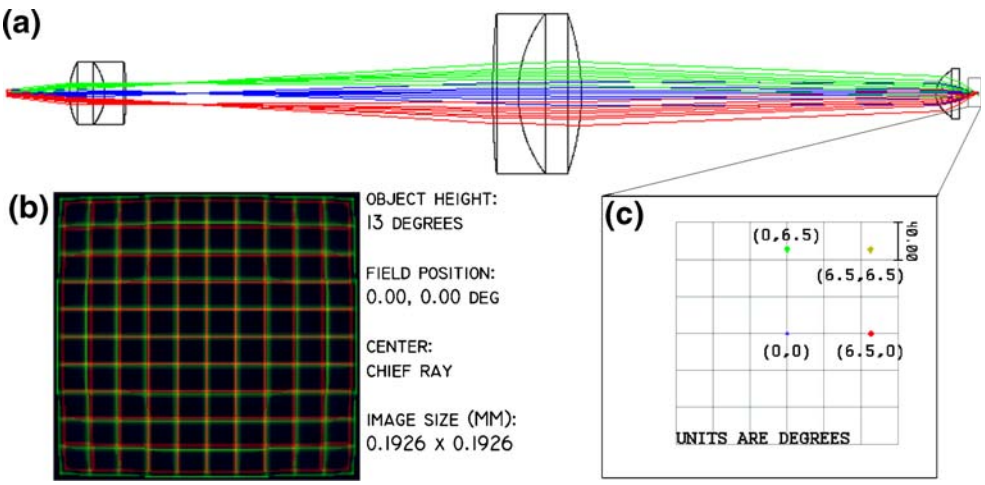

Fig. 4 Schematic of the optical layout of the distal scanning objective system simulated in ZEMAX® optical design software. (**a**) 3D layout of the micromirror scanner, afocal Keplerian beam expander (DL1-DL2), and high NA objective lens (OBJ). (**b**) Simulated lateral field of view for total micromirror optical deflection angle of 13°. (**c**) Location of four points within the field of view where optical performance is characterized

aperture of the focusing element was slightly under-filled to allow for beam scanning across the objective.

3 System characterization

3.1 Optical design simulations

Figure 4 presents the schematic of the layout of the distal-scanning objective system simulated in ZEMAX® optical design software. The simulated system (Fig. 4(a)) consists of the two-axis micromirror scanner, the afocal Keplerian beam expander (comprising lenses DL1 and DL2), and the high-NA objective lens OBJ, providing effective numerical aperture of 0.48 and working distance of 1.56 mm. For a total micromirror scanner optical deflection angle of 13°, the field of view is approximately 192×192 μm, as shown in Fig. 4(b). Detailed characterization of the system optical properties is performed for the four points within the lateral field of view indicated in Fig. 4(c); the results obtained at these four points are expected to be indicative of the performance over the entire field of view. The first set of simulations is focused on the lateral resolution characteristics of the system. Performance in this dimension is assessed by studying the spot sizes and patterns within the field of view in the sample focal plane and the modulation transfer functions at different spot locations compared against diffraction-limited performance. The results of the lateral resolution simulations are presented in Fig. 5. As evidenced from Fig. 5(a), the spot rays for all four tested locations lie within the airy disk radius, indicating that diffraction-limited performance is obtained over the entire desired field of view. Minimum spot size of 0.31 μm is obtained at the center of the field of view, while the resolution degrades to 1.092 μm at the ends of the field of view. Figure 5(b) plots the modulation transfer function (MTF) for the four locations and compares them against the diffraction-limited curve. The plots indicate that at the center of the view field, the performance is virtually indistinguishable from the ideal case, while there is a small drop in performance moving towards the edges of the field of view.

Axial performance is assessed by monitoring the spot ray diagram as the beam propagates axially through the focal plane at the four locations being tested, and by measuring the Rayleigh range of the beam. Figure 6 presents the through-focus spot diagrams for the four tested locations and the axial resolution (defined here as twice the Rayleigh range) for the beam propagating axially through the center of the field of view. The through-focus spot diagrams (Fig. 6(a)) show that the shape and extents of the spot changes quickly through even a small defocus of only 5 μm. This qualitatively indicates that the axial resolution is

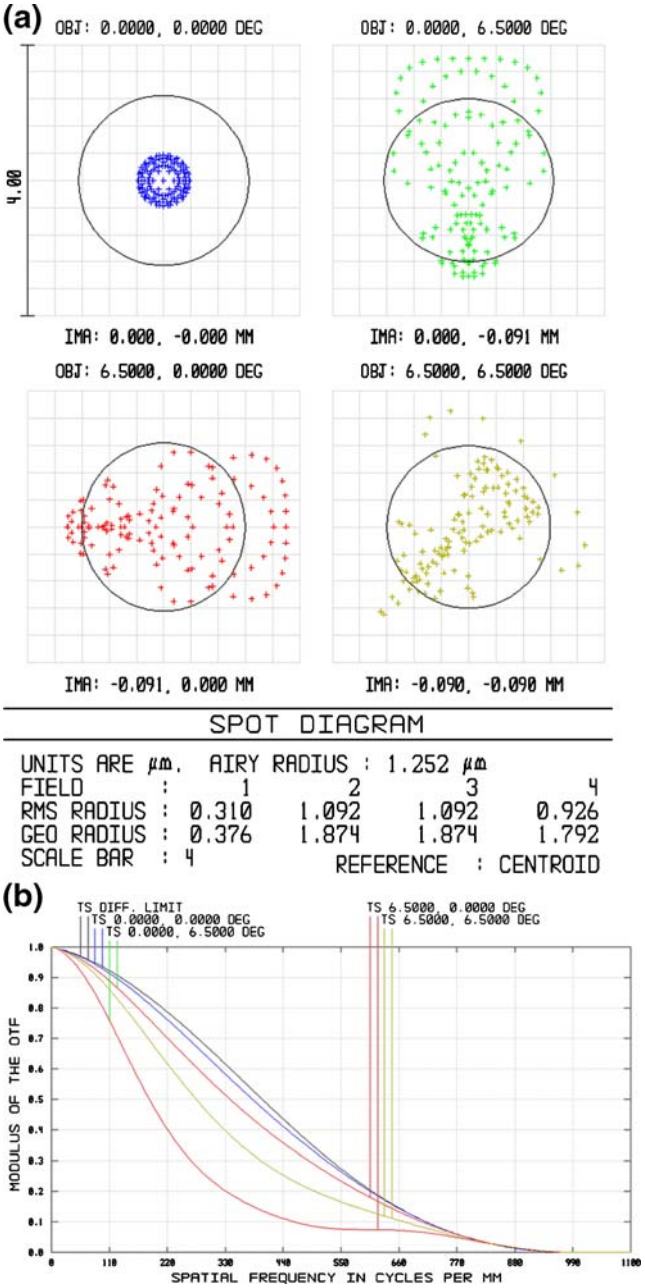

Fig. 5 Simulated lateral resolution characteristics of the distal-scanning objective system. (**a**) Spot diagram showing ray pattern and focal spot sizes in comparison with the airy disk radius. (**b**) Modulation transfer functions (MTFs) compared with diffraction-limited MTF

on the order of a few micrometers over the entire field of view. The performance is also expected to be best at the center of the field of view where the beam maintains approximately a Gaussian shape as it propagates through the sample focal plane. Figure 6(b) shows a detailed plot of the spot size of the beam as is propagates through axial the focal plane at the center of the field of view. The Rayleigh range is calculated as the distance between the z-position of

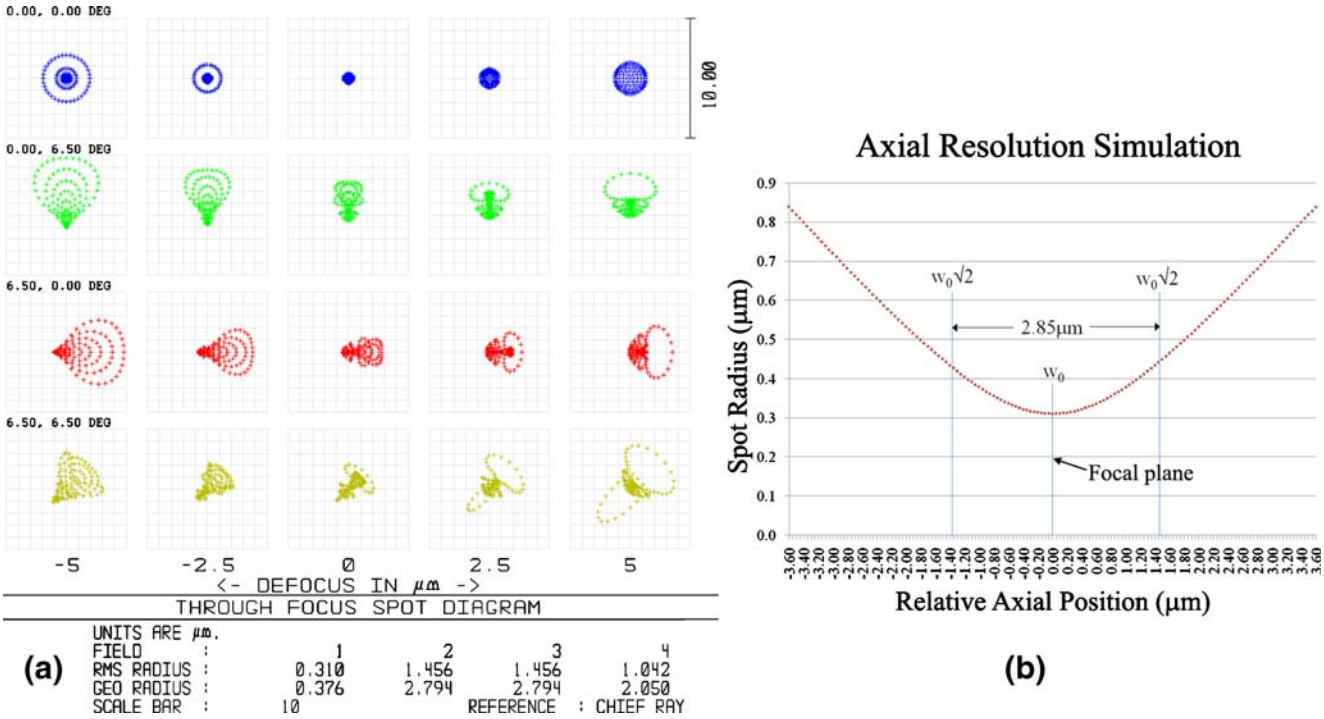

Fig. 6 Simulated axial resolution characteristics of the distal scanning-objective system. (**a**) Through-focus spot diagrams at the four tested locations in the field of view. (**b**) Plot of beam waist radius as a function of axial position relative to the focal plane measured at the center of the field of view

smallest beam waist (ω_0) to the z-position at which the waist reaches size ($\omega_0\sqrt{2}$). The axial resolution is defined here as twice the Rayleigh range, and is determined to be 2.85 μm in our case.

3.2 Experimental measurements

System resolution was experimentally determined by recording photodetector intensity against position while translating a mirror axially through the sample focal plane and a knife edge laterally in the focal plane across the beam spot. Lateral and axial resolutions were deduced from the measurement curves (Fig. 7(a–b)) using the method described in (Rajadhyaksha et al. 1999), to be 0.49 μm and 4.18 μm respectively, demonstrating our ability to achieve single-cell-layer optical sectioning that is comparable to microtome slice thickness used in conventional histology. Figure 7(c) shows an image, with 200 × 125 μm field of view, of the elements of group 7 of a standard USAF 1951 resolution target acquired using the instrument at 3.0 frames per second. The smallest elements in the image are 2.2 μm wide and spaced 2.2 μm apart.

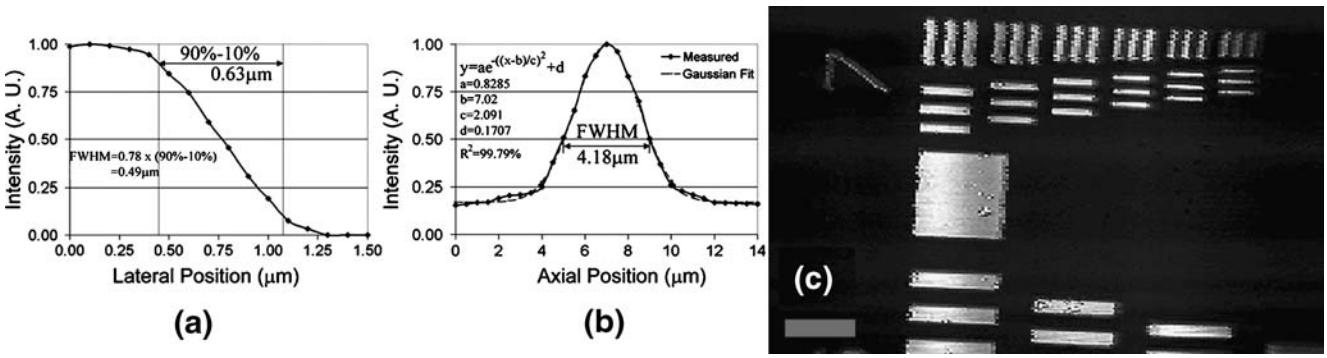

Fig. 7 Experimental measurement of the optical performance of the handheld laser-scanning confocal microscope. (**a**) Lateral resolution measurement. (**b**) Axial resolution measurement. (**c**) Image of the elements of group 7 of a USAF 1951 standard resolution target. Field of view: 200×125 μm. Scale bar: 25 μm

4 Imaging results and discussion

4.1 Reflectance confocal microscopy

We conducted experiments on *ex vivo* samples of swine liver to explore the applicability of our system to interventional imaging without the aid of contrast enhancing agents. Reflectance confocal microscopy can be extremely useful in situations where agents are not available for contrast enhancement in *in-vivo* imaging environments, and in situations where cytomorphological information can be sufficient for diagnostic purposes. All animal experiments were approved by the institutional animal care and use committee at the University of Texas M. D. Anderson Cancer Center before the start of the study. Figure 8 presents images of normal *ex vivo* swine liver obtained at different imaging depths without the use of fixing or contrast agents. Each image consists of four adjacent fields of view stitched together to form a composite image. The outermost capsular layer is depicted in Fig. 8(b). The depth of this layer is usually 1–5 cells, its structure is completely different from the underlying functional section of the organ, and serves only as a protective layer. Beneath the capsular layer, the liver consists mainly of hepatocytes, depicted in Fig. 8(c). The liver sinusoids (blood vessels) are clearly visible as white lines outlining the hepatocyte cells, and are equivalent to the white lines in Fig. 8(d), which is a bright-field image of a fixed and stained sample of the same tissue. The nuclei of the hepatocytes in Fig. 8(c), however, seem not to exhibit sufficient contrast for imaging without the aid of contrast agents.

4.2 Fluorescence confocal microscopy

The study of tumor biomarker expression via fluorescence imaging, in addition to providing useful information on cytomorphology, can provide far more powerful detail on the tumor progression and insight into treatment strategies. We chose to study the expression of cytokeratin and mammaglobin in fluorescently labeled samples of breast tissue from metastatic breast cancer patients. All patients were enrolled using protocols (IRB #092004-010) approved by the Institutional Review Board at the University of Texas Southwestern Medical Center at Dallas, and provided informed consent. On receipt, the samples were fixed in ice-cold acetone for 10 minutes, and rinsed in a mixture of phosphate buffer saline (PBS) and 0.1% Tween-20. The samples were then immersed in blocking buffer [PBS+ 0.1% Tween-20+1% Bovine Serum Albumin (BSA)] and incubated for 30 minutes at 37°C. After incubation, the samples were rinsed in PBS, blotted dry. The samples were stained with the fluorescent contrast agents conjugated to appropriate antibodies and incubated for 40 minutes at 37°C. After rinsing with PBS+0.1% Tween-20, the samples were dried, and mounting medium was added. The samples were covered with a 100 μm thick layer of polydimethylsiloxane (PDMS) infused with titanium dioxide (TiO_2) that approximates the optical scattering properties of tissue (Parthasarathy et al. 2008). The final prepared samples mimic the staining of a subsurface (100 μm depth) layer of breast tissue with fluorescent contrast agents for imaging with the handheld microscope.

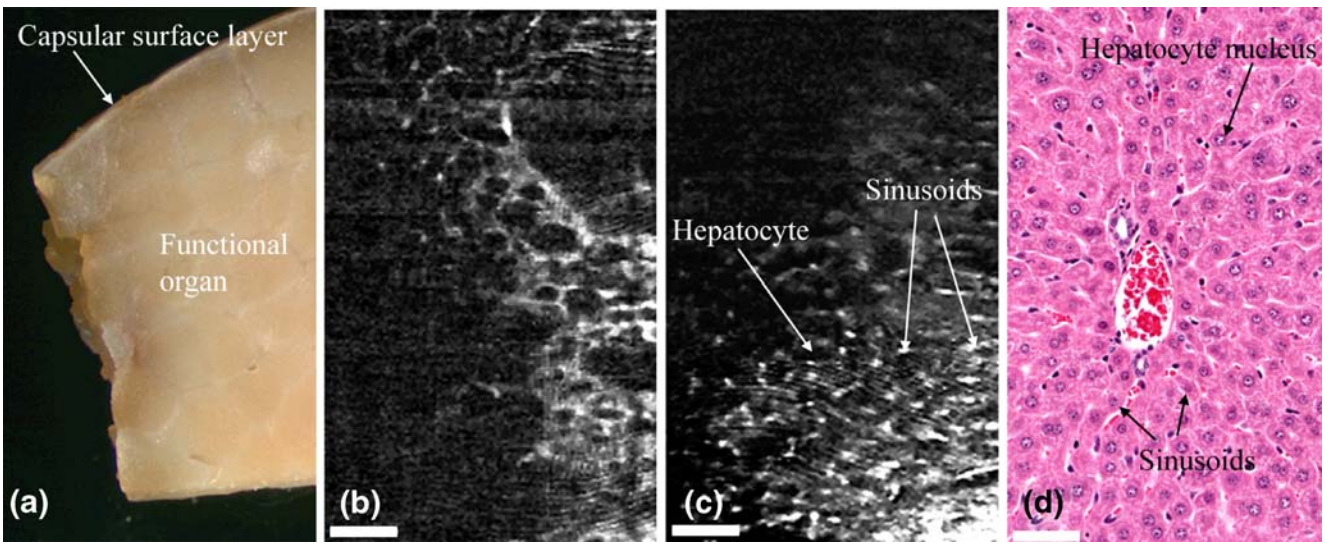

Fig. 8 Results of experiments on *ex vivo* swine liver imaging using our MEMS handheld reflectance confocal microscope. (**a**) Photomicrograph of liver sample depicting the capsular layer in relation to the rest of the organ tissue. (**b**) Image of the protective capsular layer (four fields stitched) using the MEMS instrument. (**c**) Image of hepatocyte nuclei obtained by reflectance confocal microscopy using our handheld instrument. (**d**) Bright-field image using an Olympus BX51 20× microscope of a stained swine liver tissue microtome slice. Scale bars: 50 μm

The prepared samples were first imaged under a bench-top Leica SP2 AOBS confocal microscope using a dry 0.7NA, 20× objective using 632.8 nm He-Ne laser excitation wavelength and emission filter spectra matched to the fluorophore emissions. Expression maps of the entire tissue sample were obtained from the bench-top instrument as controls for imaging with our handheld instrument. Image processing for image histogram equalization and encoding the fluorophores into color channels of the 8-bit images was performed during the imaging procedure in the proprietary software bundled with the Leica instrument. The samples were next imaged with our handheld instrument. Four fields of view were stitched together to form an image of size approximately 400×250 μm with the two fluorophores encoded into the green and red channels of the 8-bit composite color images. Image processing, including high-frequency noise removal, image histogram equalization, image rotation and resampling to match the orientation of the control images, was performed in a Matlab® programming environment.

The results of imaging three specimens obtained from metastatic breast cancer patients are presented in Fig. 9. The expression of cytokeratin and mammaglobin are depicted in sub-figures (a) and (b) respectively, while the combined overlaid control images of the expression levels, obtained from the Leica bench-top confocal microscope are presented in sub-figures (c) of each image data set. The images obtained from the MEMS handheld instrument consist of four fields of view stitched together to form a composite image spanning 400×250 μm. The control images from the Leica confocal microscope span a field of view of 750×750 μm, and contain the same 400×250 μm region of the sample imaged by the MEMS handheld instrument within them; however, the orientation and position of that region within the field of view varies between the images, as depicted by the white dashed rectangular encircled areas. The scale bar in each image data set represents 100 μm in the control (c) images, and 33 μm in the MEMS handheld instrument images (a–b). The cytokeratin expression maps are much clearer than those of mammaglobin. This may be attributed to better specific binding of the anti-cytokeratin than the antibody for mammaglobin. Interpretation of the specific meaning for the patient of these expression maps requires significant additional imaging, and analysis by a trained pathologist alongside hematoxylin-eosin stains of the same samples for comparison with the current standard of histopathological examination.

5 Conclusions

In summary, interventional imaging at improved spatial resolution complementing existing methods can be achieved employing microelectromechanical scanning mirrors as

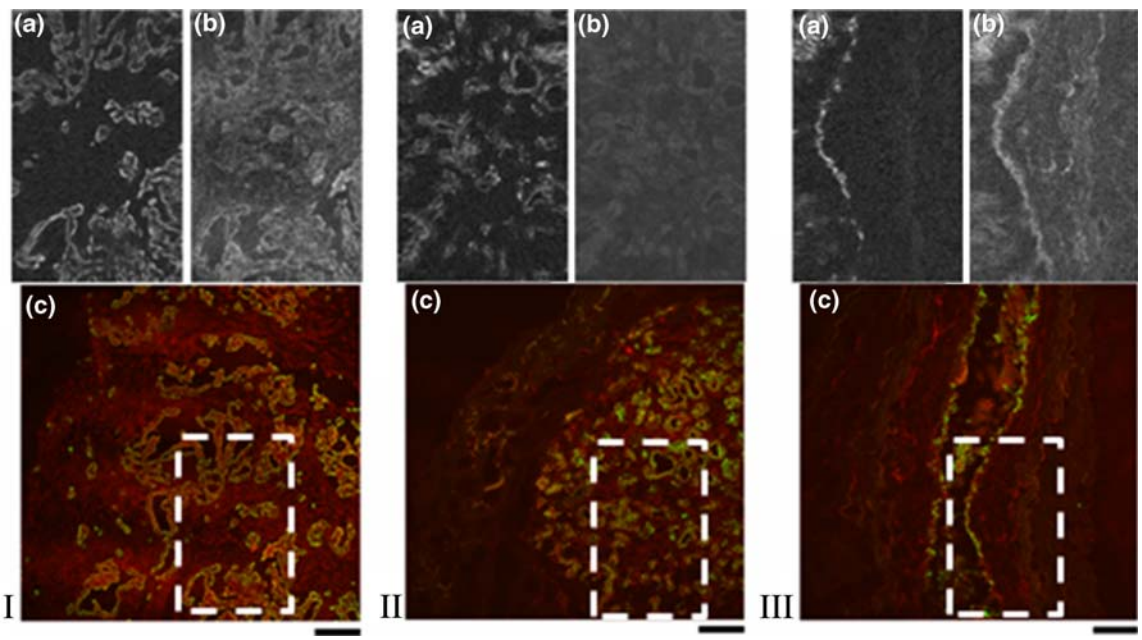

Fig. 9 Results of imaging human epithelial breast tissue from metastatic breast cancer patients using the handheld laser-scanning confocal microscope. (I-III) Image data sets from each of the three patients enrolled in the study. Images I-III (**a**) present cytokeratin expression and I-III (**b**) present mammaglobin expression. I-III (**c**) are control images obtained using Leica confocal microscope with 20× 0.7NA dry objective. Field of view for I-III (a–b): 400×250 μm (4 fields stitched); I-III (**c**): 750×750 μm. Scale bar is 100 μm for I-III (**c**), and 33 μm for I-III (a–b). White dashed rectangles indicate the areas scanned by handheld laser-scanning confocal microscope

the core technology component driving miniaturization. MEMS-based endoscope technology brings unique strength of miniaturization, batch fabrication, and integration of actuators, sensors and electronics. The combination of these features enable large array of optical devices that can be accurately positioned and assembled for compact biomedical imaging applications. The use of CMOS-compatible batch-processed microfabrication and cost-effective rapid-prototyped packaging techniques promises to enable disposable handheld probes that provide optical sectioning comparable with conventional histology. The ability to detect histologically relevant features in biological tissue by high resolution optical microscopy can prove to be a disruptive innovation that can significantly alter the technological and procedural landscape in image-guided intervention. Such tools can complement more conventional large-volume scanning systems to provide the physician with a comprehensive and detailed understanding of the physiology of the tissue to accurately assess the condition of the patient and make timely confident decisions on the basis of these diagnoses.

Acknowledgments Financial support of this research by Wallace H Coulter Foundation Early Career Award is gratefully acknowledged. The scanning micromirrors were fabricated at Stanford Nanofabrication Facility and the Microelectronics Research Center at the University of Texas at Austin, both supported by the National Science Foundation National Nanofabrication Infrastructure Network under grants 9731293 and 0335765, respectively. The University of Texas M. D. Anderson Cancer Center and University of Texas Southwestern Tissue Repository at UTSW provided the swine liver and human specimens used for this research respectively. Control images for the fluorescence microscopy experiments were obtained using equipment at the Core facilities within the Institute for Cellular and Molecular Biology at the University of Texas at Austin.

References

A.D. Aguirre, P.R. Hertz, Y. Chen, J.G. Fujimoto, W. Piyawattanametha, L. Fan, M.C. Wu, "Two-axis MEMS scanning catheter for ultrahigh resolution three-dimensional and En face imaging. Opt Express **15**, 2445–2453 (2007)

Y.-C. Cheng, C.-L. Dai, C.-Y. Lee, P.-H. Chen, P.-Z. Chang, A MEMS micromirror fabricated using CMOS post-process. Sensors and Actuators A: Physical **120**, 573–581 (2005)

D. Ching-Liang, X. Fu-Yuan, J. Ying-Zong, C. Chin-Fon, An approach to fabricating microstructures that incorporate circuits using a post-CMOS process. Journal of Micromechanics and Microengineering **15**, 98 (2005)

C.-L. Dai, F.-Y. Xiao, Y.-Z. Juang, C.-F. Chiu, An approach to fabricating microstructures that incorporate circuits using a post-CMOS process. Journal of Micromechanics and Microengineering **15**, 98–103 (2005)

H. Dooyoung, P.R. Patterson, H.D. Nguyen, H. Toshiyoshi, M.C. Wu, Theory and experiments of angular vertical comb-drive actuators for scanning micromirrors. IEEE Journal of Selected Topics in Quantum Electronics **10**, 505–513 (2004)

G.K. Fedder, R.T. Howe, L. Tsu-Jae King, E.P. Quevy, Technologies for cofabricating MEMS and electronics. Proceedings of the IEEE **96**, 306–322 (2008)

L. Fu, A. Jain, H. Xie, C. Cranfield, M. Gu, Nonlinear optical endoscopy based on a double-clad photonic crystal fiber and a MEMS mirror. Opt Express **14**, 1027–1032 (2006)

X. Gan, S.P. Schilders, M. Gu, Image enhancement through turbid media under a microscope by use of polarization gating methods. Journal of the Optical Society of America A **16**, 2177–2184 (1999)

C.L. Hoy, N.J. Durr, P. Chen, W. Piyawattanametha, H. Ra, O. Solgaard, A. Ben-Yakar, Miniaturized probe for femtosecond laser microsurgery and two-photon imaging. Opt Express **16**, 9996–10005 (2008)

C. Hyuck, D. Garmire, J. Demmel, R.S. Muller, Simple fabrication process for self-aligned, high-performance microscanners—Demonstrated use to generate a 2-D ablation pattern. Journal of Microelectromechanical Systems **16**, 260–268 (2007)

S. Kimura, T. Wilson, Confocal scanning optical microscope using single-mode fiber for signal detection. Applied Optics **30**, 2143–2150 (1991)

U. Krishnamoorthy, L. Daesung, O. Solgaard, Self-aligned vertical electrostatic combdrives for micromirror actuation. Journal of Microelectromechanical Systems **12**, 458–464 (2003)

K. Kumar, J.C. Condit, A. McElroy, N.J. Kemp, K. Hoshino, T.E. Milner, X. Zhang, Fast 3D *in vivo* swept-source optical coherence tomography using a two-axis MEMS scanning micromirror. Journal of Optics A: Pure and Applied Optics **10**, 044013 (2008a)

K. Kumar, K. Hoshino, X. Zhang, Handheld subcellular-resolution single-fiber confocal microscope using high-reflectivity two-axis vertical combdrive silicon microscanner. Biomedical Microdevices **10**, 653–660 (2008b)

K. Kumar, X. Zhang, CMOS-compatible 2-axis self-aligned vertical comb-driven micromirror for large field-of-view microendoscopes, *Proceedings of the 22nd IEEE International Conference on MicroElectroMechanical Systems (MEMS 2009)*, pp. 1015, 2009a

K. Kumar, Rony Avritscher, D.C. Madoff, X.J. Zhang, Handheld Single-Cell-Layer Optical Sectioning Reflectance Confocal Microscope for Interventional Imaging, *The 29th Conference on Lasers and Electro Optics(CLEO)*, Baltimore, Maryland, 1–5 Jun, 2009b

K.C. Maitland, H.J. Shin, H. Ra, D. Lee, O. Solgaard, R. Richards-Kortum, Single fiber confocal microscope with a two-axis gimbaled MEMS scanner for cellular imaging. Opt Express **14**, 8604–8612 (2006)

A.B. Parthasarathy, W.J. Tom, A. Gopal, X.J. Zhang, A.K. Dunn, Robust flow measurement with multi-exposure speckle imaging. Optics Express **16**, 1975–1989 (2008)

W. Piyawattanametha, R.P.J. Barretto, T.H. Ko, B.A. Flusberg, E.D. Cocker, H. Ra, D. Lee, O. Solgaard, M.J. Schnitzer, Fast-scanning two-photon fluorescence imaging based on a microelectromechanical systems two- dimensional scanning mirror. Opt Lett. **31**, 2018–2020 (2006)

H. Ra, W. Piyawattanametha, M.J. Mandella, P.-L. Hsiung, J. Hardy, T.D. Wang, C.H. Contag, G.S. Kino, O. Solgaard, Three-dimensional *in vivo* imaging by a handheld dual-axes confocal microscope. Opt Express **16**, 7224–7232 (2008)

M. Rajadhyaksha, R.R. Anderson, R.H. Webb, Video-rate confocal scanning laser microscope for imaging human tissues *in vivo*. Appl Opt **38**, 2105–2115 (1999)

J.M. Schmitt, A.H. Gandjbakhche, R.F. Bonner, Use of polarized light to discriminate short-path photons in a multiply scattering medium. Applied Optics **31**, 6535–6546 (1992)

O. Solgaard, *Photonic microsystems: Micro and nanotechnology applied to optical devices and systems*, 1st edn. (Springer, New York, 2008)

J. Woonggyu, Z. Jun, W. Lei, P. Wilder-Smith, C. Zhongping, D.T. McCormick, N.C. Tien, Three-dimensional optical coherence tomography employing a 2-axis microelectromechanical scanning mirror. IEEE Journal of Selected Topics in Quantum Electronics **11**, 806–810 (2005)

Z. Yaqoob, J. Wu, E.J. McDowell, X. Heng, C. Yang, Methods and application areas of endoscopic optical coherence tomography. Journal of Biomedical Optics **11**, 063001–19 (2006)